An equivalent lattice-modified model of interfering Bragg bandgaps and Locally Resonant Stop Bands for phononic crystal made from Locally Resonant elements

Javier Redondo [a,*], Luis Godinho [b], Kestutis Staliunas [c,d,e], Juan Vicente Sánchez-Pérez [f]

[a] Universitat Politècnica de València. Instituto de Investigación para la Gestión Integrada de zonas Costeras, Paranimf 1, Grao de Gandia, Valencia, Spain
[b] Universidade de Coimbra, ISISE, Departamento de Engenharia Civil, Rua Luis Reis Santos, 3030-788 Coimbra, Portugal
[c] Institució Catalana de Recerca i Estudis Avançats (ICREA), Passeig Lluís Companys 23, 08010 Barcelona, Spain
[d] Universitat Politecnica Catalunya (UPC), Rambla Sant Nebridi 22, 08222 Terrassa, Barcelona, Spain
[e] Vilnius University, Faculty of Physics, Laser Research Center, Sauletekio Ave. 10, Vilnius, Lithuania
[f] Universitat Politècnica de València. Centro de Tecnologías Físicas, Acústica, Materiales y Astrofísica, División acústica. Camino de Vera s/n, Valencia, Spain

ARTICLE INFO

ABSTRACT

The design and development of advanced devices based on metamaterials to control the transmission of acoustic waves is a hot topic. An important class of these metamaterials is based on phononic crystals with Locally Resonant Structure, included in those commonly known as Locally Resonant Sonic Materials. In these metamaterials, wave control is basically performed by two mechanisms: internal (or local) resonances in the scatterers that form the phononic crystal, and Bragg bandgaps due to structural periodicity. Their main control feature is the resonance peaks forming additional stop-bands away from the Bragg frequency, mainly in the low frequency regime. For some applications, coupling of the two phenomena is necessary to create a broad transmission gap. However, when both are located in close frequency ranges, some destructive interferences can occur. In this paper, the authors develop a comprehensive numerical model of periodic arrays of Hemholtz resonators, which explains in detail the physical mechanisms of this destructive interference and, simultaneously, allows the reproduction of the consequences of the interference. The numerical results are supported by experimental tests.

1. Introduction

Metamaterials are defined as artificial structures that present physical properties not found in nature. In particular, acoustic metamaterials exhibit high wave control characteristics [1–4] that enable the design of advanced devices for a large number of applications, as atenuators [5–8], antivibration systems [9,10], lenses [11] or gas sensing [12]. A particular class of these metamaterials, included in those known as Locally Resonant Sonic Materials [13–18], is based on phononic crystals formed by periodic arrays of Helmholtz Resonators (HRs) [19–24]. Here, the existence of HRs allows the sub-wavelength Locally Resonant Stop Bands (LRSBs), typically in the low frequency regimes. On the other hand, the periodicity of the structure is responsible for the formation of Bragg bandgaps (BGs). Intuitively thinking, a broad stop-band could potentially be created if both LRSBs and BGs are joined together. Such extremely broad bands would be particularly interesting for some

applications such as noise control or mechanical engineering. However, some destructive interferences appear if BGs and LRSBs are located in close frequency ranges, as has been reported in some works [25–27]. A first approach to the explanation of this BG/LRSB interference phenomenon was presented by some of us in a previous work [28], in which the main physical mechanism underlying this interference was suggested, and a simple model to partially reproduce its effect was proposed.

Here the authors present a comprehensive model that explains and reproduces this interference phenomenon in a general way, including the cases analyzed in previous works and extended by other ingredients such as the orientation of the HR aperture or the relative position of BG/LRSB in the frequency domain. A simplified numerical model has been built based on the Boundary Elements Method (BEM), taking into account the thermoviscous losses and supporting the results obtained with accurate laboratorial experiments performed under controlled

conditions. The model has been developed using different two-dimensional samples of a particular type of phononic crystal formed by rigid scatterers in air [29–31].

2. Numerical model

For the BEM model used in this work, the classic Helmholtz equation is solved, accounting for the linear acoustic response of the system,

$$\Delta p + k_0^2 p = 0 \tag{1}$$

where $\Delta = \partial^2/\partial x^2 + \partial^2/\partial y^2$ and $k_0 = \omega/c_0$, ω being the angular frequency and c_0 the sound propagation velocity. To solve this governing equation, a classic BEM is applied, in the form of the boundary integral equation,

$$c\, p(x_0) = -i\rho_0\omega \int_\Gamma G(x,x_0)v(x,\overrightarrow{n})d\Gamma - \int_\Gamma H(x,x_0,\overrightarrow{n})p(x)d\Gamma + p_{inc}(x_f,x_0) \tag{2}$$

where ρ_0 is the density of the medium, $p(x)$ is the acoustic pressure at point x along the boundary Γ, $v(x,\overrightarrow{n})$ is the particle velocity at x in the outward pointing normal direction $(\overrightarrow{n})$, c is a constant equal to 0.5 for smooth boundary segments, and $G(x,x_0)$ and $H(x,x_0,\overrightarrow{n})$ are the Green's functions in terms of pressure and of its derivative, i.e. the fundamental solutions excited by a point source at x; $p_{inc}(x_f,x_0)$ accounts for possible sources within the domain. Further details of this formulation can be found for instance in [32].

A sketch of the model is presented in Fig. 1a, in which periodic boundary conditions are imposed on the top and bottom boundaries, whereas the absorbing boundary conditions are considered on the left and right boundaries. To account for the effect of possible thermal and viscous losses occurring along the boundaries of the sonic crystal's scatterers, a special boundary condition is imposed, in the form of a Boundary Layer Impedance (BLI). Several possibilities exist, such as those proposed by Bossart [33] or Schmidt [34]; in this work, the Wentzel-type boundary condition proposed by Berggren [35] is used,

$$-\delta_V \frac{i-1}{2}\Delta_T p + \delta_T k_0^2 \frac{(i-1)(\gamma-1)}{2}p + \frac{\partial p}{\partial n} = 0 \tag{3}$$

where Δ_T represents the sum of the second order spatial derivatives in the tangent directions; δ_V and δ_T are the viscous and thermal acoustic boundary-layer thicknesses, respectively, which can be defined as (ν being the kinematic viscosity of air),

$$\delta_V = \sqrt{\frac{2\nu}{\omega}}\,\delta_T = \sqrt{\frac{2\lambda}{\omega\rho_0 C_p}} \tag{4}$$

It should be noted that the indicated BLI condition is only valid when, in the case of narrow paths, there is no overlapping of the viscous or thermal layers associated to neighbouring surfaces (a detailed discussion on this point can be found in [36]). For the different geometries analysed in the present paper, this condition was always fulfilled.

To obtain the results presented throughout this paper, the BEM was implemented using quadratic discontinuous elements, with 3 internal nodes per element, which allow evaluating the second order spatial derivatives required in Equation (3) in a simple manner.

The geometry of the BEM model is also shown in Fig. 1a. The two-dimensional computational domain of length L = 1 m includes rigid scatterers (from 1 to 3) with external (internal) radius r_{ext} (r_{int}). This model works with arrays of Closed Cylinders (CC), which serve as a reference, or with cylindrical HRs with length and cross-sectional area of the neck, A_n and L_n respectively. The scatterers are separated by the lattice constant of the square array, lc. In a previous work [28] two orientations of the HRs neck, 0° (HR0°) and 180° with respect to the direction of an incident plane wave travelling from left to right were considered, showing that the insulation behaviour of both HRs arrays was exactly the same. However, in order to expand the scope of the previous model, the 90° orientation of the HRs (HR90°) has been also considered here. A scheme of the geometry of the different scatterers used is given on the right of Fig. 1a, with the specific geometrical values of the model: lc = 0.085 m; r_{ext} = 0.0633 m; r_{int} = 0.0417 m; d = 0,5 m; L_n = 0.0108 m and A_n = 0.015 m. With these specifications, BG and LRSB are around 2000 Hz and 1000 Hz respectively. However, a small variation in the position of the LRSB in the frequencies domain can be observed in Fig. 1a depending on the orientation of the HR neck [37].

The effect of the destructive BG/LRSB interference is apparent in Fig. 1b, which shows the BGs in HR0° (blue dotted line) that was analyzed in [28], and HR90° (red dotted line) cases, compared to the reference case with CC, where no interference between the two band gaps was identified. It can be seen that in both HRs situations the BG/LRSB interference causes two effects in the BG with respect to the CC
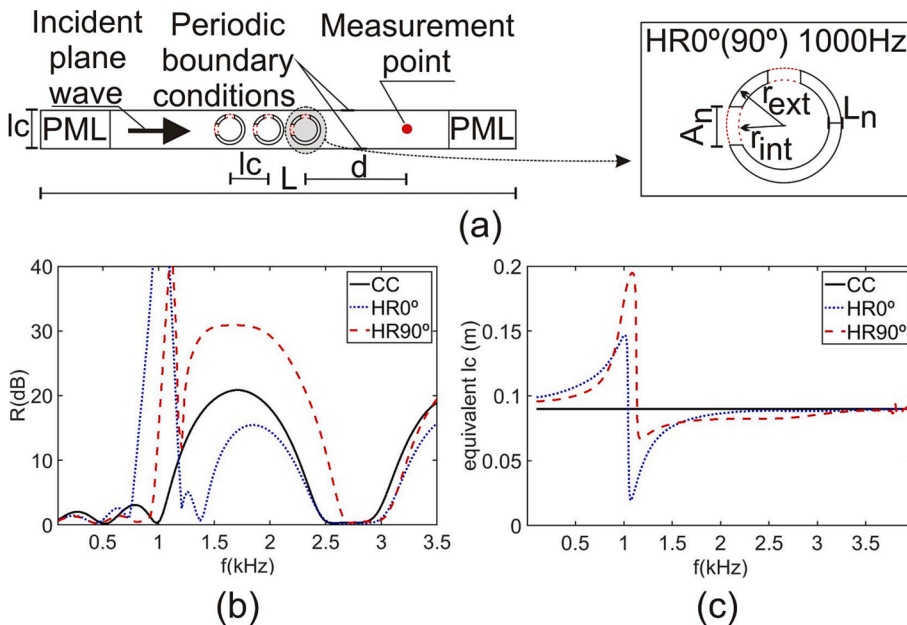

Fig. 1. (a) Scheme of the BEM model to explore the destructive BG/LRSB interference. The different types of CCs/HRs scatterers used are presented on the right; (b) Numerical insulation spectra showing the destructive interferences BG/LRSB for HR0° (blue dotted line) and HR90° (red dashed line) arrays with LRSB located below BG in the frequency range. The array of CCs, in which there is no interference, (black continuous line) appears as a reference; (c) Variation of the equivalent lattice constant in the direction of wave propagation, lc_x, as a function of the frequency due to HR-induced phase shift for arrays formed by HR0° and HR90°.

case,

(i) its displacement in the frequencies range;
(ii) a variation in its width.

In the previous paper, the authors concluded that the displacement is related to the phase shift produced by the HRs in the transmitted wave. As shown in Fig. 1c, this phase shift can be interpreted as a change in the lattice from its actual value, lc = 0.17 m, in the direction of the propagation of the wave, OX. Therefore, an equivalent lattice constant in that direction, lc_x, can be defined as a function of frequency, which would successfully explain this part of the interference phenomenon. One should note, however, that the second effect of the of the BG/LRSB interference, corresponding to the variation in the BG insulation level, cannot be explained using this approach.

3. Numerical analysis

To define a model that can successfully account for the variation in the insulation level occurring in the BG due to the BG/LRSB interference, an analysis of the insulation produced by a single row of scatterers located in the perpendicular direction to the wave propagation in the BEM model has been carried out, and is shown in Fig. 2a; this corresponds to removing rows 2 and 3, for the cases CC, HR0° and HR90°, and the dependency on the lattice constant lc_x is thus eliminated. Fig. 2a shows that the insulation of the HR0° case (blue dotted line) presents a slight increase below the LRSB and a decrease above it with respect to the reference case with closed cylinders (CC, black solid line), whereas the HR90° case (red dashed line) shows an opposite trend. This interpretation following from the same reasoning as in [28] justifies just the displacement of the BG in the frequency domain. Thus, the actual behaviour can be related either to the variation of the radii of the scatterers or to the variation of the equivalent lattice constant in the direction perpendicular the incident wave, hereafter lc_y (not to confuse with the lattice constant in the forward direction of the wave, lc_x, whose variation is responsible for the displacement of the BG).

The variation of the scatterer radii in the single rows considered,

keeping lc_y constant, is presented in Fig. 2b, where several different calculations of a single row formed by CC varying their radii (dashed black lines) were superimposed with the insulation spectra shown in Fig. 2a. First, the radii of the scatterers have been varied by ± 25%. The use of this parameter does not allow obtaining single CC equivalent rows that reproduce the insulation behaviour of the HRs arrays, mainly due to the lack of insulation variation that occurs especially around 3000 Hz (Fig. 2b). On the other hand, some results of the insulation achieved by single CC rows varying lc_y by ± 25% and keeping the radii of the scatterers constant are presented by black dashed lines in Fig. 2c, superimposed with the insulation spectra shown in Fig. 2a. From the intersections of the insulation spectra for HR0° and HR90° cases with the estimated CC ones, it is possible to approximate the equivalent lattice constant in the OY direction, lc_y, of a CC row that presents the same insulation than the HR0° and HR90° cases for each frequency. The result is shown in Fig. 2d, where the variation of the equivalent lc_y around its real value as a function of frequency for both HR0° and HR90° cases is presented. As an example, the red circles in Fig. 2c and 2d show the intersections of two single-row CC insulation curves with that of the HR90° case together with their corresponding equivalent lc_y values.

Application of the model of single rows to the case of arrays is further explored in Fig. 3. The upper part of Fig. 3a represents the variation of both the equivalent lc_x and lc_y as a function of frequency for HR0° (lc_x by blue continuous line and lc_y by blue dotted line) and for HR90° (lc_x by red continuous line and lc_y by red dashed line) arrays. Analyzing this figure, it follows that the variation trend of the equivalent lc_x and lc_y is different according to (i) the orientation of the HRs' necks and (ii) the OX/OY directions. From these values, at the bottom of Fig. 3a, the equivalent CC arrays calculated for both cases (HR0° in blue circles and HR90° in red circles) at three frequencies (marked by vertical black dotted lines in the upper part of the figure) is shown. Note that for the first case considered (200 Hz), the equivalent CC arrays for the HR0° (blue cylinders) and HR90° (red cylinders) cases are almost the same as the original ones. This means that for frequencies far away from the resonance peak, the lc change induced by the HRs is negligible. However, for the following two cases (850 Hz and 1400 Hz), at frequencies closely above and below the resonance frequency, the equivalent CC
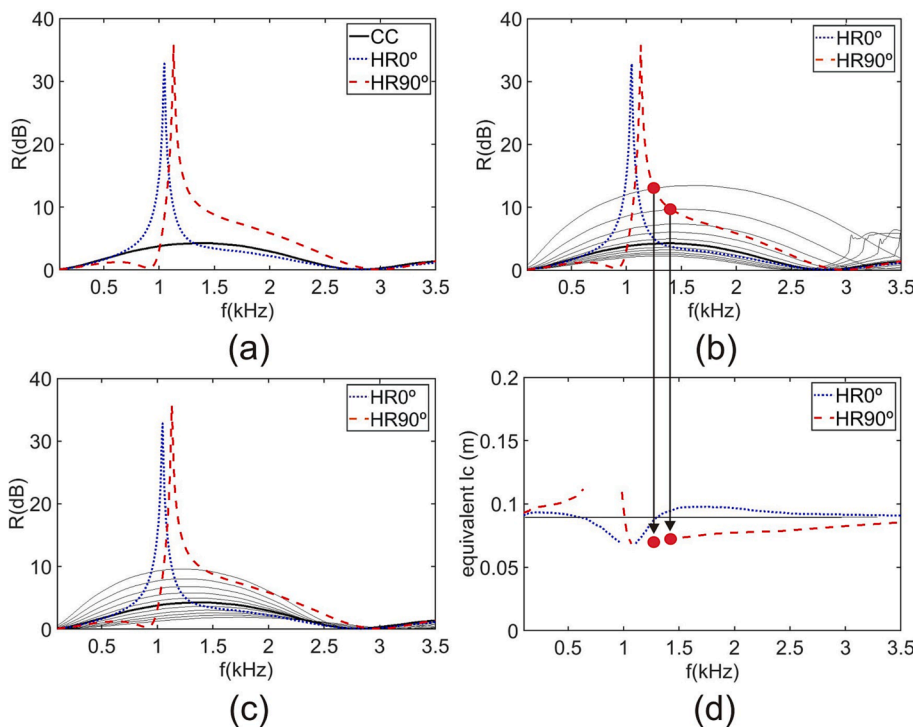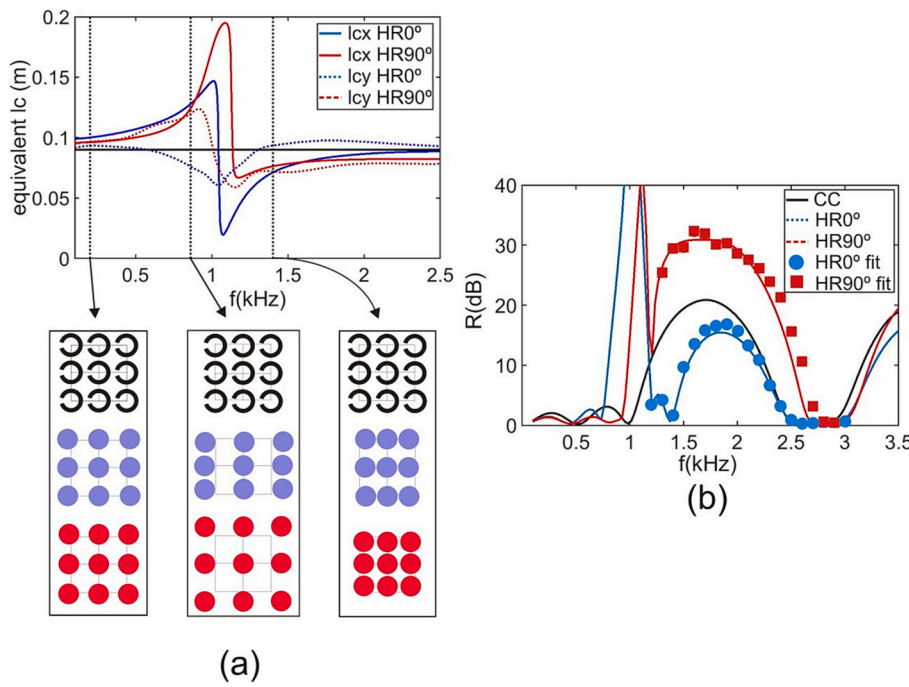

Fig. 2. (a) Insulation spectra for a single row directed perpendicular to the wave propagation direction, as a function of frequency: CC (black continuous line), HR0° (blue dotted line) and HR90° (red dashed line); the same figure but including different insulation spectra obtained for single CC rows by varying (b) the radius of the scatterers, (c) the lattice constant in OY direction, lc_y; (d) variation of the equivalent lc_y obtained from the previous figure for both HR0° (blue dotted line) and HR90° (red dashed line) rows. The red circles in Fig. 2c and 2d illustrate, as an example, the approach followed to obtain the equivalent lc_y values.

Fig. 3. (a) Variation of the equivalent lc$_x$ and lc$_y$ as a function of frequency for the starting HR0° and HR90° arrays, calculated according to our approach. The lc value of the starting square array is shown as a reference (black continuous line). Three examples of equivalent CC arrays formed with the corresponding equivalent lc$_x$ and lc$_y$ for different frequencies can be seen at the bottom of the figure. The starting HR0° array is represented as an eye guide in black; b) Numerical simulation of the insulation versus frequency, showing the destructive BG/LRSB interference for HR0° (dotted blue line) and HR90° (red dashed line) cases. Different numerical values of the insulation have been added, obtained with the proposed model, using the corresponding equivalent CC arrays for HR0° (blue circles) and HR90° (red squares) cases.

arrays are deformed by the HRs in both OX and OY directions.

These results explain the complete BG/LRSB interference phenomenon as a change of the equivalent lattice constant produced by the HRs in the two directions of the original HRs array. This can be confirmed in Fig. 3b, where the insulation values for the different equivalent arrays of CC, calculated as a function of frequency (blue circles for HR0° and red squares for HR90°), are plotted, together with the simulations of the destructive BG/LRSB interference for both HRs cases, already reported in Fig. 1b. A very good agreement between both types of simulations is observed.

4. Validation and numerical experiments

In order to validate these calculations experimentally, a set of measurements in an anechoic chamber of dimensions 8.00 × 6.00 × 3.00 m3 have been carried out as summarized in Fig. 4. A prepolarized free-field 1/2″ microphone Type 4189B&K and a directional sound source GENELEC 8040A emitting continuous white noise, located at 1 m from the sample have been used. The position of the microphone is determined by using a Cartesian robot, called three-dimensional Robotised e-Acoustic

Measurement System (3DReAMS) [38]. This robot is capable of sweeping the microphone through a 3D grid of measuring points located at any trajectory inside the chamber. The microphone acquires the temporal signal when the robotised system is turned off. Then the signal is saved and the frequency response of the measured sample is obtained using the Fast Fourier Transform (FFT). For both the data acquisition and the motion of the robot, National Instruments cards PCI-4474 and PCI-7334 have been used together with the Sound and Vibration Toolkit and the Order Analysis Toolkit for LabVIEW. A picture of 3DReAMS is shown at the upper part of the Figure First, the insulation spectra for the CC, HR0° and HR90° cases have been measured with the original lc$_x$ and lc$_y$ values (lc$_x$ = lc$_y$ = 0.17 m).

These measurements demonstrate experimentally the existence of the BG/LRSB interference previously shown by BEM simulations. Furthermore, in order to validate our comprehensive model, the insulation of several equivalent CC arrays determined by varying their equivalent lcx and lcy has been measured for both HR0° and HR90° cases. A good agreement between these values and the insulation spectra obtained for the HR0° and HR90° starting arrays can also be observed, which supports our model. The possible difference between the
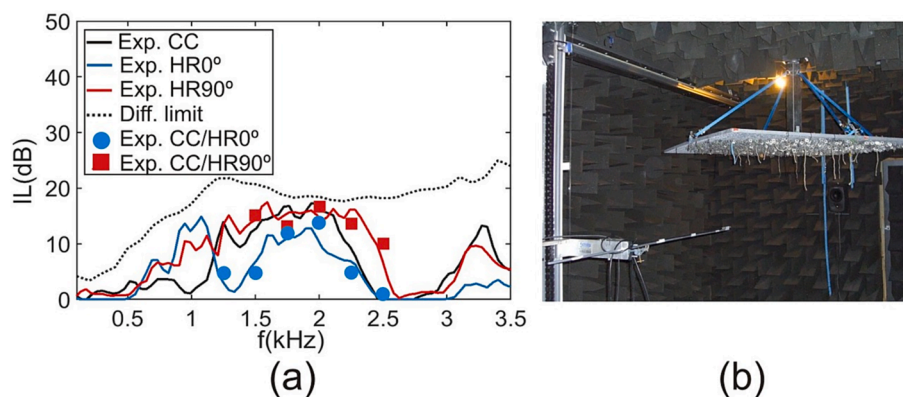

Fig. 4. A) experimental insulation spectra versus frequency showing the destructive bg/lrsb interference for hr0° (blue continuous line) and hr90° (red continuous line). experimental insulation values for some equivalent cc arrays following the model proposed have been measured for hr0° (blue circles) and hr90° (red squares) cases. the diffraction limit due to the finite size of the samples is also represented (black dotted line). b) a picture of the experimental setup used is shown in the inset.

numerical and experimental results can be explained by the finite size of the sample considered, which implies the appearance of a diffraction limit, understood as the maximum insulation value that can be obtained for these finite samples.

Finally, to show the robustness of the proposed model, Fig. 5 shows its applicability to three different cases in which the relative positions of BG and LRSB in the frequency domain are varied, verifying its results against those provided by the complete BEM model, including the resonant elements.

In Fig. 5a results are presented for the case, already analysed, in which the LRSB is below the BG in the frequency domain (BG≈2000 Hz and LRSB≈1000 Hz). On the left side of the figure the simulated values of the equivalent lc_x and lc_y for the HR0° and HR90° cases can be seen, as a function of frequency. On the right side, the simulated insulation spectra of the starting CC, HR0° and HR90° arrays are plotted, together with the insulation results of some equivalent CCs arrays calculated following this model. In addition, Fig. 5b and 5c represent the results where there is an overlap in the position of BG and LRSB (BG≈2000 Hz and LRSB≈1600 Hz) and where LRSB is above BG in the frequency domain (BG≈2000 Hz and LRSB≈2200 Hz), respectively. A good agreement is observed between the results of both the HR0° and HR90° cases with the equivalent arrays formed by CCs, showing the suitability of the model.

5. Conclusions

In the present paper, the authors presented a complete model that successfully explains and reproduces the interference between the Bragg Bandgap and the Local Resonance Stop Bands in acoustic metamaterials consisting of phononic crystals formed by periodic arrays of Helmholtz resonators. This interference has a double effect on the Bragg Bandgap of these metamaterials: (i) a displacement in the frequency domain and (ii) a variation in its insulation level. In a preceding work it was proved that the displacement of the Bragg Bandgap can be understood as a virtual change in the lattice constant of the array in the direction of the propagating wave, and allows the definition of an equivalent lattice constant in that direction, lc_x, which exactly reproduces this phenomenon. In the same line, the variation in the insulation level of the Bragg Bandgap can be explained as the lattice constant change however in the direction perpendicular to the direction of the wave, lc_y. In order to generalise the proposed model, which postulates the existence of equivalent arrays of closed cylinders formed with equivalent lattice constants, lc_x and lc_y, it has been successfully applied to three cases where the relative Bragg Bandgap/Local Resonance Stop Bands position has been varied. The numerical results obtained show the robustness of the proposed model. The numerical simulations performed for the formalisation of the model have been validated with accurate experiments under controlled conditions. The results obtained may help to improve the design of
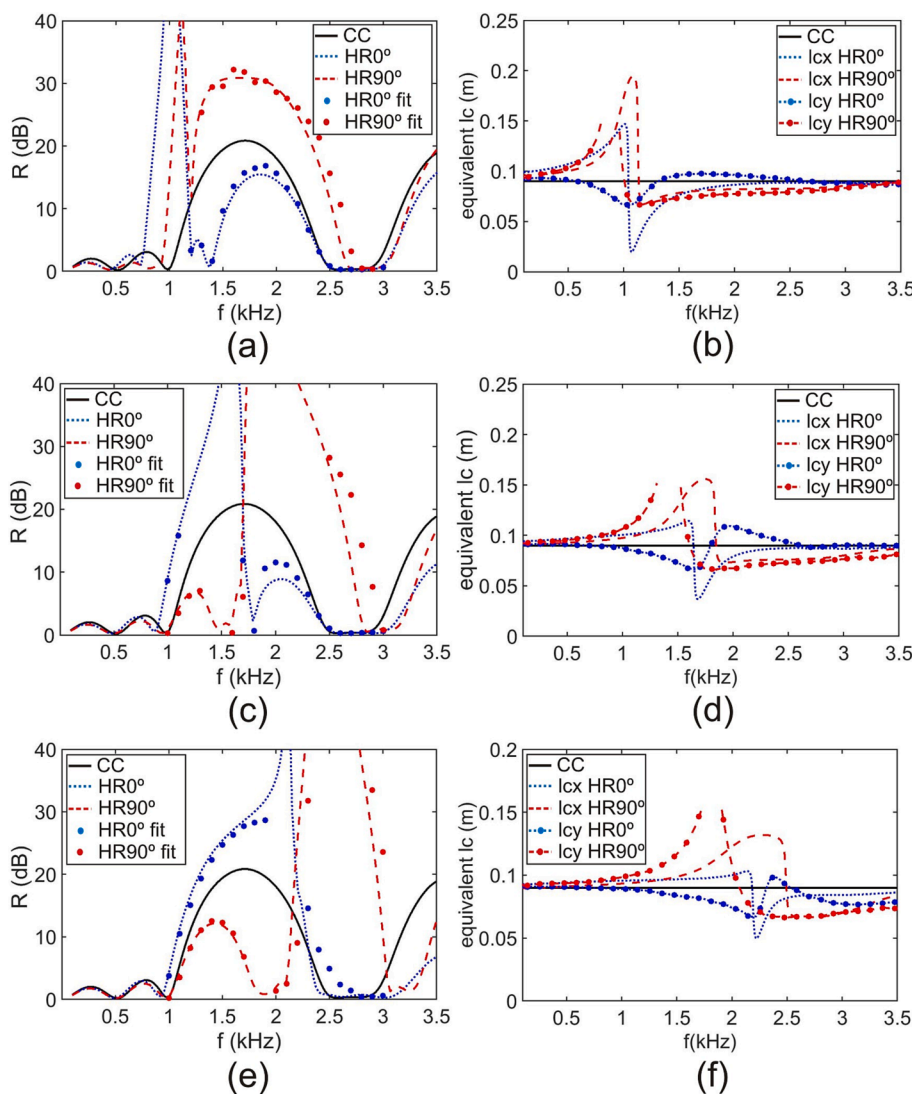

Fig. 5. Application of the comprehensive model to three different cases of interference as a function of the relative position of the BG/LRSB in the frequency domain. On the left is plotted the variation of the equivalent lc_x and lc_y as a function of frequency for the HR0° and HR90° cases. On the right the insulation spectra is shown for the CC (black solid line), HR0° (Blue dotted line) and HR90° (red dashed line) cases, together with the results of the adjustment performed following the proposed model for both HR0° (blue circles) and HR90° (red squares) arrays; (a) LRSB below BG (LRSB≈1000 Hz and BG≈2000 Hz); (b) LRSB/BG overlapping (LRSB≈1600 Hz and BG≈2000 Hz); (c) LRSB above BG (LRSB≈2000 Hz and BG≈2200 Hz).

advanced technological devices for wave control based on this kind of metamaterials.

CRediT authorship contribution statement

Declaration of Competing Interest

The authors declare the following financial interests/personal relationships which may be considered as potential competing interests: Javier Redondo reports financial support was provided by Ministry of Science Technology and Innovations. Kestutis Staliunas reports financial support was provided by Ministry of Science Technology and Innovations. Luis Godinho reports financial support was provided by European Regional Development Fund.

Data availability

Data will be made available on request.

Acknowledgements

Appendix A. Supplementary data

Supplementary data to this article can be found online at https://doi.org/10.1016/j.apacoust.2023.109555.

References

[1] Li J, Chan CT. Double-negative acoustic metamaterial double-negative acoustic metamaterial. Phys Rev E 2004;70(5):055602.

[2] Fok L, Ambati M, Zhang X. Acoustic metamaterials. MRS Bull 2008;33(10):931–4.

[3] Vasileiadis T, Varghese J, Babacic V, Gomis-Bresco J, Navarro Urrios D, Graczykowski B. Progress and perspectives on phononic crystals. Journal of Applied Physics 2021;129(16):160901.

[4] Kumar S, Pueh Lee H. Recent advances in active acoustic metamaterials. Int J Appl Mech 2019;11(08):1950081.

[5] Mei J, Ma G, Yang M, Yang Z, Wen W, Sheng P. Dark acoustic metamaterials as super absorbers for low-frequency sound. Nat Commun 2012;3(1):1–7.

[6] Leroy V, Strybulevych A, Lanoy M, Lemoult F, Tourin A, Page JH. Superabsorption of acoustic waves with bubble metascreens. Phys Rev B 2015;91(2):020301.

[7] Du Y, Wu W, Chen W, Lin Y, Chi Q. Control the structure to optimize the performance of sound absorption of acoustic metamaterial: A review. AIP Advances 2021;11(6):060701.

[8] Mi Y, Lu Z, Yu X. Acoustic inerter: ultra-low frequency sound attenuation in a duct. J Acoust Soc Am 2020;148(1):EL27–32.

[9] Meng H, Bailey N, Chen Y, Wang L, Ciampa F, Fabro A, Chronopoulos D, Elmadih W. 3D rainbow phononic crystals for extended vibration attenuation bands. Sci. Rep. 2020;10:18989.

[10] Hu B, Zhang Z, Yu D, Liu J, Zhu F. Broadband bandgap and shock vibration properties of acoustic metamaterial fluid-filled pipes. Journal of Applied Physics 2020;128(20):205103.

[11] Tang, K., Qiu, C., Lu, J., Ke, M., Liu, Z. (2015). Focusing and directional beaming effects of airborne sound through a planar lens with zigzag slits. *Journal of Applied Physics, 117*(2), 024503.

[12] Kaya OA, Korozlu N, Trak D, Arslan Y, Cicek A. One-dimensional surface phononic crystal ring resonator and its application in gas sensing. Applied Physics Letters 2019;115(4):041902.

[13] Liu Z, Zhang X, Mao Y, Zhu YY, Yang Z, Chan CT, et al. Locally resonant sonic materials. Science 2000;289(5485):1734–6.

[14] Mehaney A, Ahmed AM. Locally resonant phononic crystals at low frequencies based on porous SiC multilayer. Sci Rep 2019;9(1):1–12.

[15] Gorshkov V, Sareh P, Navadeh N, Tereshchuk V, Fallah AS. Multi-resonator metamaterials as multi-band metastructures. Materials & Design 2021;202:109522.

[16] Tang YF, Liang B, Yang J, Yang J, Cheng JC. Topological phononic crystals with tunable interface state based on local resonance. Applied Physics Express 2019;12(9):094002.

[17] Mohapatra K, Jena DP. Insertion loss of sonic crystal made with multi resonant shells. Applied Acoustics 2021;171:107676.

[18] Radosz J. Acoustic performance of noise barrier based on sonic crystals with resonant elements. Appl Acoust 2019;155:492–9.

[19] Hu X, Chan CT, Zi J. Two-dimensional sonic crystals with Helmholtz resonators. Phys Rev E 2005;71(5):055601.

[20] Cai X, Guo Q, Hu G, Yang J. Ultrathin low-frequency sound absorbing panels based on coplanar spiral tubes or coplanar Helmholtz resonators. Applied Physics Letters 2014;105(12):121901.

[21] Cavalieri T, Cebrecos A, Groby JP, Chaufour C, Romero-García V. Three-dimensional multiresonant lossy sonic crystal for broadband acoustic attenuation: Application to train noise reduction. Appl Acoust 2019;146:1–8.

[22] Ning L, Wang YZ, Wang YS. Active control of elastic metamaterials consisting of symmetric double Helmholtz resonator cavities. Int J Mech Sci 2019;153:287–98.

[23] Krasikova, M., Baloshin, Y., Slobozhanyuk, A., Melnikov, A., Powell, D., Petrov, M., & Bogdanov, A. (2020, December). Noise reduction using structures based on coupled Helmholtz resonators. In *AIP Conference Proceedings* (Vol. 2300, No. 1, p. 020069). AIP Publishing LLC.

[24] Ma K, Tan T, Yan Z, Liu F, Liao WH, Zhang W. Metamaterial and Helmholtz coupled resonator for high-density acoustic energy harvesting. Nano Energy 2021;82:105693.

[25] Karimi M, Croaker P, Kessissoglou N. Acoustic scattering for 3D multi-directional periodic structures using the boundary element method. J Acoust Soc Am 2017;141(1):313–23.

[26] Montiel F, Chung H, Karimi M, Kessissoglou N. An analytical and numerical investigation of acoustic attenuation by a finite sonic crystal. Wave Motion 2017;70:135–51.

[27] Cenedese M, Belloni E, Braghin F. Interaction of Bragg scattering bandgaps and local resonators in mono-coupled periodic structures. Journal of applied physics 2021;129(12):124501.

[28] Peiró-Torres MP, Castiñeira-Ibáñez S, Redondo J, Sánchez-Pérez JV. Interferences in locally resonant sonic metamaterials formed from Helmholtz resonators. Applied Physics Letters 2019;114(17):171901.

[29] Economou EN, Sigalas MM. Classical wave propagation in periodic structures: Cermet versus network topology. Phys Rev B 1993;48(18):13434–8.

[30] Martínez-Sala R, Sancho J, Sánchez-Pérez JV, Gómez V, Llinares J, Meseguer F. Sound attenuation by sculpture. Nature 1995;378:241.

[31] Fredianelli L, Ginevra Del Pizzo L, Licitra G. Recent Developments in Sonic Crystals as Barriers for Road Traffic Noise Mitigation. Environments 2019;6(2):14.

[32] Wu, T. W. (Ed.). (2002). Boundary element acoustics fundamentals and computer codes.

[33] Bossart R, Joly N, Bruneau M. Hybrid numerical and analytical solutions for acoustic boundary problems in thermo-viscous fluids. J Sound Vib 2003;263(1):69–84.

[34] Schmidt K, Thöns-Zueva A. Impedance boundary conditions for acoustic time-harmonic wave propagation in viscous gases in two dimensions. Mathematical Methods in the Applied Sciences 2022;45(12):7404–25.

[35] Berggren M, Bernland A, Noreland D. Acoustic boundary layers as boundary conditions. J Comput Phys 2018;371:633–50.

[36] Duclos A, Lafarge D, Pagneux V. Transmission of acoustic waves through 2D phononic crystal: visco-thermal and multiple scattering effects. Eur Phys J Appl Phys 2009;45(1):11302.

[37] Agudelo, D. M. G., Jeong, C. H., Andersen, P. R., Henriquez, V. C. (2020). Angle-dependent Absorption Property of 2D Infinite Periodic Arrangements of Helmholtz Resonators. In *Forum Acusticum 2020* (pp. 1033-1039).

[38] Romero-Garcia V, Sánchez-Pérez JV, Garcia-Raffi LM. Evanescent modes in sonic crystals: Complex dispersion relation and supercell approximation. Journal of Applied Physics 2010;108:044907.